PAPER • OPEN ACCESS

3D printed elastomers with superior stretchability and mechanical integrity by parametric optimization of extrusion process using Taguchi Method

View the article online for updates and enhancements.

You may also like

Materials Research Express

PAPER

3D printed elastomers with superior stretchability and mechanical integrity by parametric optimization of extrusion process using Taguchi Method

Abbas Bayati[1] , Mina Ahmadi[2], Davood Rahmatabadi[1] , Mohammad Khodaei[3], Hao Xiang[4], Majid Baniassadi[1] , Karen Abrinia[1], Ali Zolfagharian[5] , Mahdi Bodaghi[6] and Mostafa Baghani[1]

1   School of Mechanical Engineering, College of Engineering, University of Tehran, Tehran, Iran
2   School of Automotive Engineering, Iran University of Science and Technology, Tehran, Iran
3   Materials Engineering Group, Golpayegan College of Engineering, Isfahan University of Technology, Golpayegan, 87717-67498, Iran
4   College of Civil Engineering and Architecture, Southwest University of Science and Technology, Sichuan, 621010, People's Republic of China
5   School of Engineering, Deakin University, Geelong, 3216, Australia
6   Department of Engineering, School of Science and Technology, Nottingham Trent University, Nottingham, NG11 8NS, United Kingdom

E-mail: mahdi.bodaghi@ntu.ac.uk and baghani@ut.ac.ir

Abstract

This study focused on a modified Fused Deposition Modeling (FDM) 3D printing method, specifically the direct pellet printing of a propylene-based thermoplastic elastomer, Vistamaxx™ 6202, to address challenges like printability and weak mechanical properties. The main objective was optimizing printing parameters and investigating their impact on the mechanical properties. The Taguchi method was used to design the experiments, reducing the required experiments and optimizing printing parameters to maximize desired properties. Three influential parameters were chosen, each changing to three levels. By employing the Taguchi method, the number of experiments decreased from 27 full factorials to 9. Regression models were created through analysis of variance (ANOVA) and verified by additional experiments. Tensile tests were performed according to the ASTM D638 standard. SEM imaging was used to assess interlayer adhesion and structural integrity. The results demonstrated satisfactory interlayer adhesion and structural integrity of the printed samples. Notably, the printed thermoplastic elastomers achieved significant stretchability, reaching up to 5921.3%. The tensile strength was 5.22 MPa, with a tensile modulus of 1.7 MPa. The effect of each parameter and their contribution percentage to the tensile strength, elongation, and elastic modulus were obtained from the variance analysis.

1. Introduction

Elastomers are a class of polymers with unique mechanical properties, such as high flexibility, good impact resistance, and chemical resistance. These properties make elastomers suitable for various applications. The use of elastomers for high-tech applications, including wearable devices [1, 2], soft robotics [3], and medical industries [4], has been increasing rapidly in recent years. Parida *et al* [5] have developed a composite material based on thermoplastic elastomer, liquid metal, and silver flakes. This composite material exhibits high conductivity, extreme stretchability, and healability, making it suitable as a stretchable conductor in triboelectric nanogenerators. Duduta *et al* [6] have developed a soft composite dielectric elastomer actuator (DEA) using strain-stiffening elastomers and carbon nanotube electrodes. They have achieved a peak energy density of 19.8 J kg^{-1}, close to the upper limit for natural muscles. That study's low-density, ultrathin carbon nanotube electrodes could sustain high electric fields without dielectric breakdown.

Additive manufacturing (AM), or 3D printing, has revolutionized the manufacturing industry by providing an efficient and cost-effective approach to producing complex parts with intricate geometries [7–9]. AM has

been widely used to make various materials [10, 11]. However, this technology has been challenging to apply to the printing of elastomers. [12]. Such challenges in printing elastomers arise from their unique properties, such as high elasticity and low viscosity. For instance, selecting the right powder for printing elastomers is a significant challenge in Selective Laser Sintering (SLS). To achieve optimal printing results, it is essential to choose powders with high stiffness and low adhesion properties. Furthermore, [13] powders with spherical shapes are preferred, as they facilitate smooth flow during the printing process [14].

Fused Deposition Modeling (FDM) is a popular AM technique that involves the layer-by-layer deposition of a polymeric material to create a 3D object [15, 16]. FDM is one of the most widely used AM techniques due to its numerous advantages over other AM techniques [17]. FDM is relatively simple and cost-effective compared to other methods, such as Stereolithography (SLA) and Selective Laser Sintering (SLS) [18, 19]. FDM printers are available in a wide range of prices and sizes, making the technology accessible to small businesses and individuals [20]. Additionally, FDM printers require minimal post-processing, which reduces the overall cost and time needed to produce a part. Printing elastomers using FDM presents a unique set of challenges, some specific to the printing technology, while others are specific to the printed elastomeric materials. The most challenging part of FDM printing of elastomers is extrusion failure mechanisms. These can occur due to improper filament diameter, buckling, or annular backflow [14]. Notably, commercially available TPU and TP filaments have been shown to exhibit excellent printing capabilities. However, it's important to acknowledge that these commercial filaments often contain additives to enhance their printability. To overcome these challenges, various techniques have been developed for printing elastomers. Khondoker *et al* [21] addressed a common issue in 3D printing by securing the extruder onto the printer frame and guiding the material through a heated tube to the nozzle. This innovative technique eliminates the need for a filament. It also enables printing extremely soft materials with a shore hardness below 60 A, which is currently the lowest limit for commercially available FFF materials. The researchers successfully demonstrated the efficacy of this method by producing a pneumatic finger using styrene-ethylene-butylene-styrene thermoplastic elastomer, which had a shore hardness of approximately 47 A.

Eliminating filament by directly printing elastomer pellets can be an effective way to print elastomers easily [22]. Direct pellet printing, or fused granular fabrication (FGF), is a type of FDM process that involves using pellets of elastomeric material. These pellets are melted and extruded through a nozzle to create the desired shape [23]. This method is highly efficient for elastomer and soft material printing as it does not involve utilizing filament, thus avoiding associated problems. Furthermore, this method uses commercially available and inexpensive elastomer pellets [24].

The inherent properties of some elastomers, such as being thermoset, present other challenges for their processing and recycling, especially in AM. Thermoset elastomers undergo a chemical cross-linking reaction during processing, which imparts superior mechanical properties, but also results in irreversibly fixed shapes that cannot be reprocessed. This presents a significant environmental challenge as these materials cannot be recycled, leading to increased waste and pollution [25]. In contrast, thermoplastic elastomers (TPEs) are a type of elastomer that can be melted and reprocessed multiple times, making them a more sustainable alternative to thermoset elastomers [26]. TPEs have similar mechanical properties to thermoset elastomers and can be formulated to achieve a wide range of hardness, making them suitable for various applications. The use of TPEs in 3D printing has gained attention in recent years due to their environmentally friendly and cost-effective nature [27]. Pawar *et al* [28] introduced a new method for controlling the properties of 3D-printed thermoplastic elastomer foam specimens. The researchers used a foamable filament made of a thermoplastic elastomer and thermally expanded microspheres (TEMs) to investigate how different material extrusion printing parameters affect the material density. Specifically, they analyzed the impact of nozzle temperature and diameter on the material density. The researchers concluded that as the content of thermally expanded microspheres (TEMs) in the filament increases, the density reduction of 3D-printed samples also increases. They also found that the main factor controlling the density reduction is the nozzle temperature of the printer.

Propylene-based thermoplastic elastomers (PBEs) are a particular type of TPE with favorable properties and are commercially available as pellets [29]. Vistamaxx™ 6202, a well-known PBE produced by ExxonMobil (USA), is primarily composed of isotactic propylene (85 wt%) repeat units with a random ethylene distribution (15 wt%) created using metallocene catalyst technology. The unique microstructure of these PBEs includes physical cross-links between hard segments with either a high melting temperature or a high glass transition temperature (Tg) and soft segments with a low Tg. This results in both the elasticity of traditional elastomers and the recyclability of thermoplastics. Under strain-induced deformation, the soft segments elongate, while the hard parts act as anchoring points for elastic recovery. In previous studies, propylene-based thermoplastic elastomers like Vistamaxx™ 6202 have been primarily used as tougheners in blends or as elastic matrices for composites. Wang *et al* [30] used this material as a toughener and investigated the overall performance change of a high-flow polypropylene by adding three different types of polyolefin-based elastomers (PBEs). They examined the chain microstructures of PBEs and analyzed their mechanical, thermal, and optical properties, as well as the morphology of the blends with polypropylene. The results showed that all three types of PBEs

effectively improved the Izod impact strength of the polypropylene blends by incorporating rubber compositions, although stiffness was reduced. Cvek *et al* [31] used Vistamaxx as a matrix material to fabricate magnetorheological elastomers (MREs) due to its advantageous characteristics as a thermoplastic elastomer without the limitations associated with conventional chemically cross-linked elastomers. They demonstrated the concept of reprocessing MREs for the first time. By subjecting this material to three successive reprocessing cycles using injection molding, they observed a significant decrease in the relative magnetorheological (MR) effect attributed to reduced particle mobility.

The Taguchi method is considered one of the best experimental methodologies used to determine the minimum number of experiments that need to be performed within the permissible limits of factors and levels. This method offers an effective and reliable approach to simplifying the feasibility of a study and experimental plan for different process parameters. This is particularly important in AM technologies, where the cost of producing the products is still high. There are several research studies have utilized the Taguchi method to optimize and enhance the performance of the FDM process [32–34]. Deng *et al* [35] utilized the Taguchi method to design an L_9 orthogonal array to study the effects of four parameters: printing speed, layer thickness, printing temperature, and filling ratio. Each parameter was tested at three different levels to analyze its impact on the tensile properties of PEEK samples printed using FDM. The optimal results were obtained when the printing temperature was set to its highest level and the layer thickness was set to its lowest level. The other two factors were set at their middle level (level 2). Liu *et al* [36] also used the Taguchi method to analyze the effects of five parameters (build orientation, layer thickness, raster width, air gap, and raster angle) on the impact, flexural, and tensile strengths of ABS printed parts via FDM. They observed that build orientation was the most significant parameter, followed by layer thickness and raster angle.

There is a clear need to optimize printing parameters for elastomers, especially with new methods like direct pellet printing. Printing thermoplastic elastomers can be challenging, but direct pellet printing offers solutions. However, changes in different printing parameters can greatly affect the mechanical properties of the printed elastomers. When multiple parameters interact, it becomes more difficult to select the best combination. Therefore, it is important to conduct optimization studies for this new technique to improve its effectiveness and performance. This study uses Vistamaxx™ 6202 as the primary material for the FDM direct pellet extrusion process. To our knowledge, there are no existing reports on optimizing printing parameters for this specific soft and stretchable thermoplastic elastomer material. Therefore, it is crucial to study and optimize the printing parameters and their effect on the mechanical properties of printed parts. In this study, the mechanical properties of the printed parts were optimized based on printing parameters such as printing speed, nozzle diameter, and nozzle temperature. The Taguchi method was employed to design the experiments and determine the optimal printing parameters that maximize the desired properties (Ultimate Tensile Strength (UTS), Elongation (El), and Young's Modulus (E)). Finally, regression models were created, and their feasibility was tested by two additional tests. The development of a low-modulus TPE through printing is a pioneering approach that can potentially guide the development of printing techniques for conductive elastomers, highly stretchable sensors, and wearable devices. Furthermore, since this material has not been printed before, it is crucial to investigate the effects of printing parameters on its mechanical properties, which can have a significant impact on its performance.

2. Materials and methods

2.1. Materials
In this study, a propylene-based thermoplastic elastomer pellet (trade name Vistamaxx™ 6202, ExxonMobil, USA), was used as the feedstock material for direct pellet 3D printing. The material specifications are summarized in table 1.

2.2. 3D Printing
In this study, we utilized a modified FDM 3D printer for the direct pellet printing of elastomeric material. This printer was created by replacing the filament feeding system in a commercial FDM printer with a lab-made direct pneumatic feeding system. This model is very suitable for printing soft thermoplastics and elastomers. Creating filaments for elastomers is difficult because it is hard to produce round and uniform filaments from these materials. Often, the filaments have different diameters along their length or an elliptical shape. This inconsistency can disrupt the printing process or cause the filaments to break. Another significant challenge in printing with elastomeric filaments using commercially available systems is filament buckling. This problem occurs because elastomeric filaments have a relatively low stiffness. In a typical FFF printer, there is a roller feeding system and a heated nozzle that are spaced apart. Filaments tend to bend as they pass through the drive wheels or gears. If the filament is not fed correctly into the system, it can fall into the gap between the drive gears
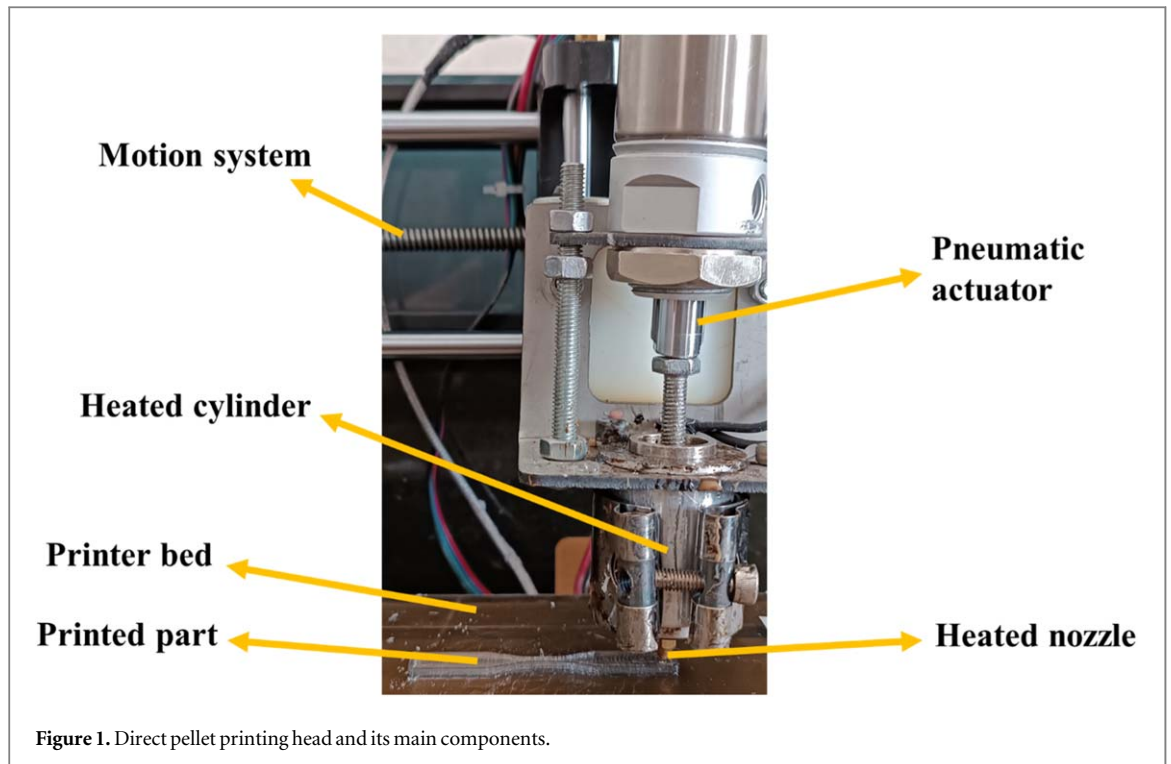
Figure 1. Direct pellet printing head and its main components.

Table 1. Specifications Vistamaxx^{TM} granules as feedstock material.

Appearance/form	Transparent/pellets
Density (g/cm^3)	0.862
Hardness (shore A)	64
Ethylene content (%)	15
Melt Flow Index (g/10 min)	9.1
Melt-Mass-Flow Rate (MFR) (g/10 min)	20

and the nozzle inlet. Additionally, if the filaments become tangled or twisted, they are likely to get stuck in this gap. Moreover, if the speed of the drive gear is faster than the rate at which the filament is extruded, a compressive force can be applied to the filament, causing it to buckle under pressure.

In this lab-made printer model, the elastomer material is poured into a cylinder that leads to the nozzle. The material is then melted in the cylinder using heaters and extruded from the heated nozzle with the pressure generated by the piston, which is driven by a pneumatic actuator. The flow of material can be controlled by adjusting the pneumatic pressure behind the piston. The other components of a typical commercial FDM printer, such as the table and motion system, remain unchanged. The 'Simplify 3D' slicer software was employed for the 3D printing process. Figure 1 depicts the printing head used in this study, highlighting its constituent parts.

2.3. Parameters selection

There are various parameters affecting the FDM process and the properties of the printed parts, including the nozzle diameter, extrusion temperature, infill density, raster angle, layer thickness, pattern, and printing velocity. In this study, based on the authors' previous studies and experiences [37], three variables of nozzle diameter, extrusion temperature, and printing velocity were selected to be studied in terms of their effects on the properties of the final printed parts when each variable is changed at three levels (see table 2).

Other printing parameters which were set to be constant during the process are summarized in table 3. The parameters listed in tables 3 and 2 were selected based on the authors' prior experience and expertise in printing with this material, ensuring that the experimental conditions were optimized for obtaining meaningful results [38]. The raster angle was chosen as 0/90. The reason for this choice is to obtain an optimal and balanced state between tensile strength and elongation [39].

Some of the parameters presented in tables 2 and 3 are illustrated schematically in figure 2. Figure 2(a) shows a side view, while figure 2(b) provides a top view of the printed part.
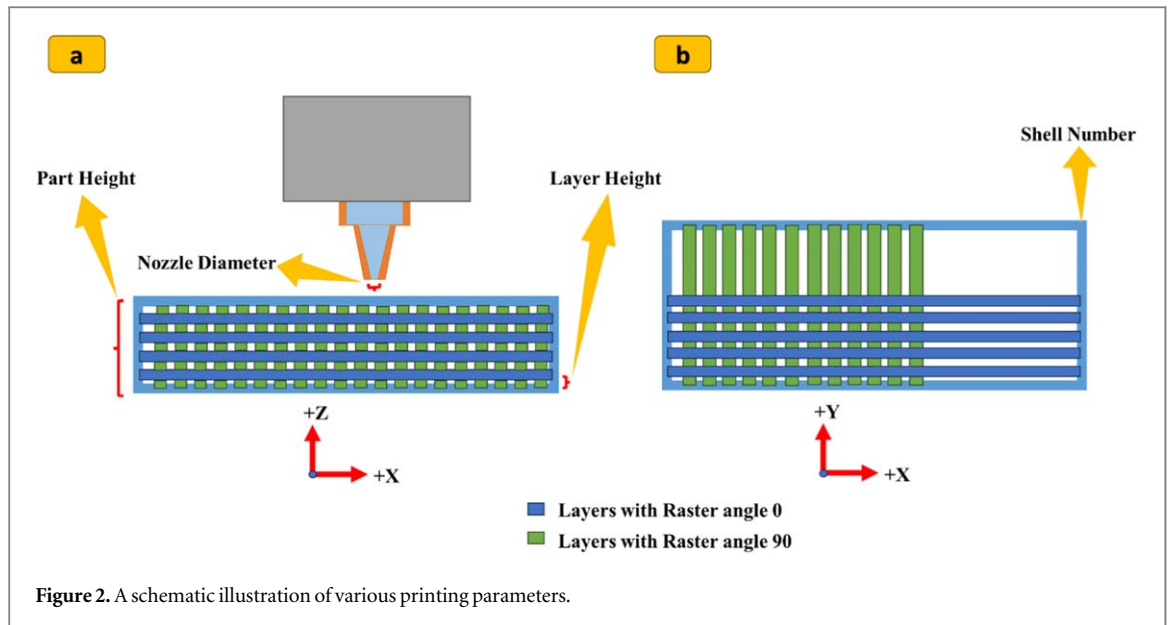
Figure 2. A schematic illustration of various printing parameters.

Table 2. FDM controllable parameters and their levels.

symbol	FDM parameters	Coded levels			Unit
		1	2	3	
A	Nozzle Diameter	0.4	0.6	0.8	mm
B	Extrusion Temperature	180	195	210	(°C)
C	Printing Velocity	2	6	10	mm/s

Table 3. Printing parameters.

Layer height (mm)[a]	0.2,0.4,0.6
Infill density (%)	100
Raster angle (°)	0/90
Shell number	1
Bed temperature (°C)	65

[a] Layer height/thickness is changed based on the nozzle diameter, so as there are three nozzle diameters, 3 different layer heights are obtained.

2.4. Design of experiment (DOE)

Design of Experiments (DOE) is a branch of applied statistics that deals with planning, conducting, analyzing, and interpreting controlled tests to evaluate the factors that control the value of a parameter or group of parameters. DOE is a powerful data collection and analysis tool that can be used in a variety of experimental situations. It allows for multiple input factors to be manipulated to determine their effect on a desired output (response). By manipulating multiple inputs simultaneously, DOE can identify important interactions that may be missed when experimenting with one factor at a time. All possible combinations can be investigated (full factorial) or only a portion of the possible combinations (fractional factorial). There are various DOE methods, such as full factorial designs, fractional factorial designs (Screening designs), Response Surface Methodology (RSM), mixture designs, Taguchi array designs, and split-plot designs.

2.4.1. Taguchi method

Design of Experiments using the Taguchi method is a standardized form of experimental design technique (referred to as classical DOE). The Taguchi method uses a fractional factorial design known as an orthogonal array (OA) to determine the impact of parameters and optimal combinations with fewer experiment runs. It consists of three steps: 1. Design of experiments, 2. Analysis of Variance (ANOVA), and 3. Optimization.

Table 4. Designed and proposed an L$_9$ orthogonal array by the Taguchi method, input factors, their levels, and their set.

Number of runs	Input factors and their levels (L9 Taguchi Design)		
	Factor A: Nozzle Diameter (mm)	Factor B: Temperature (°C)	Factor C: Velocity (mm/s)
1 (1-1-1)	1	1	1
2 (1-2-2)	1	2	2
3 (1-3-3)	1	3	3
4 (2-1-2)	2	1	2
5 (2-2-3)	2	2	3
6 (2-3-1)	2	3	1
7 (3-1-3)	3	1	3
8 (3-2-1)	3	2	1
9 (3-3-2)	3	3	2

In the first step, a series of experiments is designed and recommended using the Taguchi method to analyze the effects of various factors on process performance while reducing the number of required experiments. This study involves three factors, each with three levels. Using the Taguchi orthogonal array, two options are proposed: L$_9$ and L$_{27}$. The L$_9$ array involves 9 experiments, whereas the L$_{27}$ array represents a full factorial design with 27 experiments. To minimize the number of experiments, the L$_9$ array was selected, and table 4 was created accordingly. Table 4 outlines the combinations of factors and their corresponding levels. For instance, run 8, represented as 3-2-1, indicates that the first factor (nozzle diameter) is set to its third level (0.8 mm), the second factor (extrusion temperature) is at its second level (195 °C), and the third factor (printing velocity) is at its first level (2 mm s^{-1}). By employing orthogonal arrays (OAs), all factors are systematically tested across all levels, enabling an efficient and comprehensive evaluation of their effects on process performance. This structured approach ensures the effective identification of the most significant factors influencing the results.

By creating a table of designed experiments, tests are conducted and the results for each experiment are recorded. The next step in Taguchi design is the analysis of variance, or ANOVA, which is a statistical tool used to identify significant factors or parameters, calculate each factor's contribution, and separate noise from the signal. In the ANOVA section (tables A1–A3) provided by software such as Minitab, one can determine which parameters have the most significant impact on the results and their individual contributions. Tables A1–A3 contains important information, with the P-value and contribution percentages being the most crucial. The P-value indicates the model's efficiency, while the contribution percentages show how much each factor affects the results.

The next part of Taguchi design and analysis is signal-to-noise (S/N) ratio analysis, which is a key performance measure in the Taguchi method. In this step, the robustness of the model is measured to determine how well a process is performed in relation to its variability, aiming to make the system less sensitive to noise (uncontrollable factors). S/N is also used for optimizing the model and process based on the following calculations:

1. Smaller-the-Better: Used for characteristics where lower values are preferred.

2. Larger-the-Better: Used for characteristics where higher values are better.

3. Nominal-the-Best: Used for characteristics where the target value is ideal, and deviations are undesirable.

The optimization step is the final stage in which the optimal levels of the factors based on the S/N ratio analysis are identified, and regression models are created. Additional experiments can be conducted for validation and verification of the suggested models.

This study utilizes the Taguchi method for designing the experiments, reducing the number of experiments, and optimizing the process parameters. Three factors of Nozzle Diameter (mm), Nozzle Temperature (°C), and Printing Velocity (mm/s) are considered to be studied in terms of their impacts on the process results, including UTS (MPa), El (%), and E (MPa).

Each input factor is set to be changed in three levels. However, using a full factorial 3factoe-3level design experiments to only 9, using L$_9$ orthogonal array. Table 4 shows the input variable and their levels, as well as the suggested L$_9$ orthogonal array by the Taguchi design.
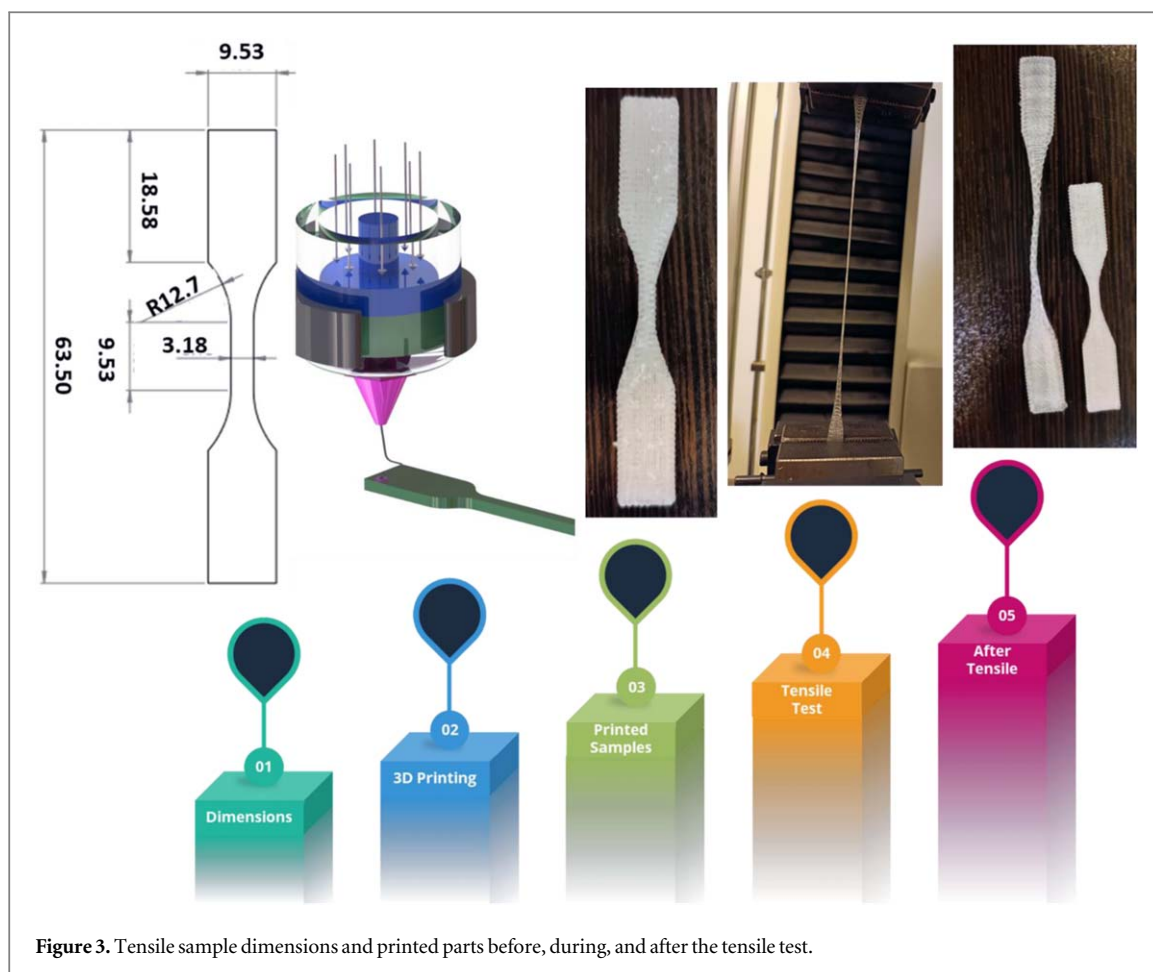
Figure 3. Tensile sample dimensions and printed parts before, during, and after the tensile test.

2.5. Tensile test

A series of tensile tests were performed to assess how different printing parameters impact the mechanical properties of 3D printed elastomers, specifically their stretchability, Young's modulus, and tensile strength. Dog bone-shaped specimens were printed according to the ASTM D638 type V standard, with both consistent and variable printing parameters. The details of these parameters are provided in table 2.

The tensile test was conducted using a SANTAM STM50 mechanical tester with a load cell capacity of 100 kg. The test was performed at room temperature with a 100 mm min^{-1} strain rate until failure occurred. The strain-stress curves were recorded for a minimum of 3 specimens, and the average values are presented in the results. Figure 3 illustrates the dimensions of the tensile samples and the printed parts before, during, and after the tensile test.

2.6. SEM imaging

Scanning electron microscopy (SEM) was used to examine the interlayer adhesion and structural integrity of samples with optimal and worst printing parameters. Our objective was to analyze the bonding between layers by studying the fracture cross-sections using SEM. A two-step preparation procedure was followed to ensure accurate analysis and enhance imaging resolution.

In the first stage, the samples were fractured in a controlled environment of liquid nitrogen. This approach allowed us to obtain clean and well-defined fracture surfaces, which are essential for obtaining reliable microstructural data. In our study, we prepared an additional dog-bone-shaped sample for each printing parameter and conducted SEM imaging on these samples. The freeze-fracture was performed in a direction perpendicular to the sample. Specifically, the clamping area was included in the fracture plane, allowing us to capture the detailed morphology of the fracture surface.

Next, a thin layer of gold coating was applied to the fractured samples. The gold coating served multiple purposes. Firstly, it provided electrical conductivity to the samples, reducing charging effects during SEM imaging. Additionally, the gold coating improved surface contrast and resolution, making it easier to visualize microstructural features.
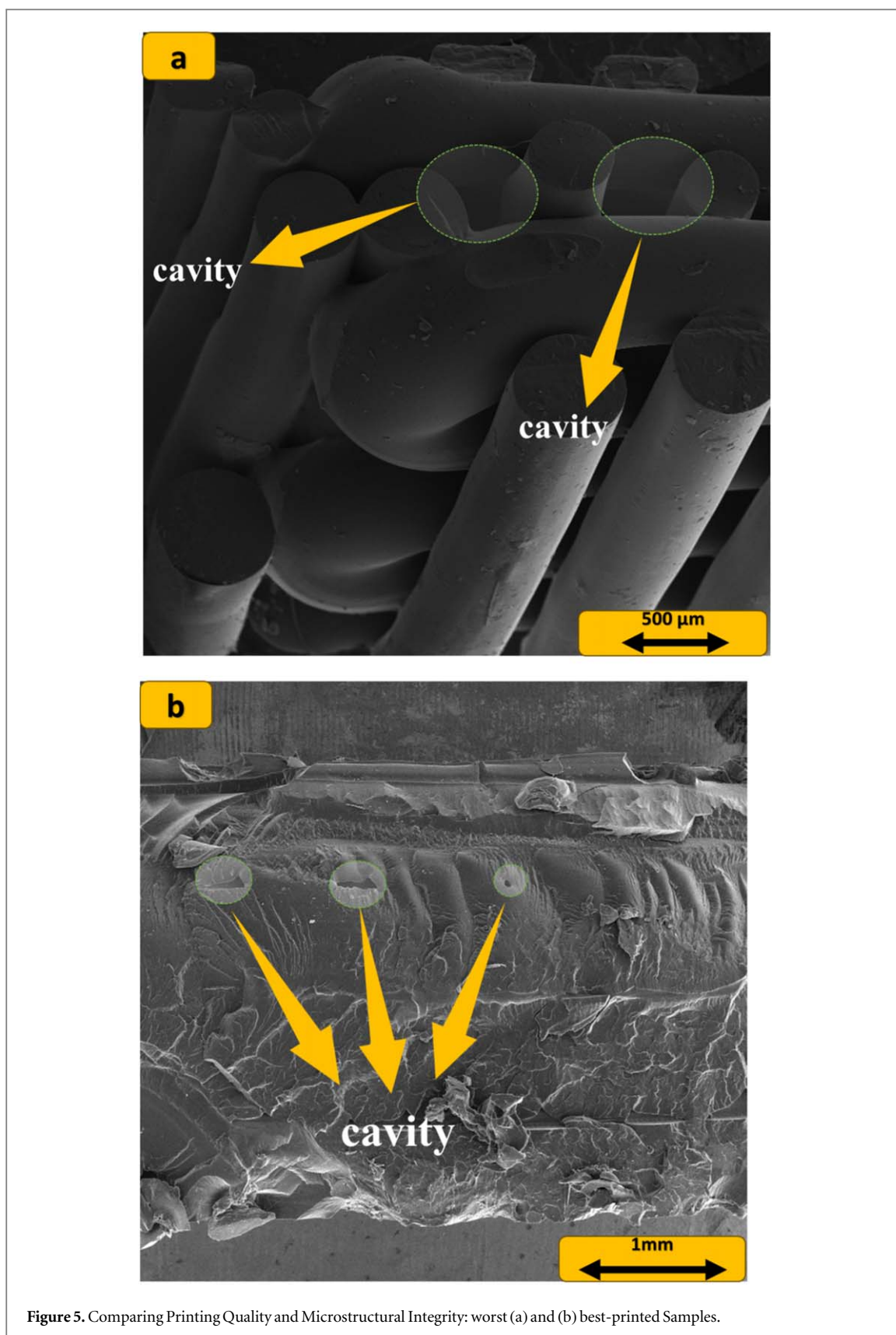
Figure 4. Cavities between layers in cross-section of a printed part.
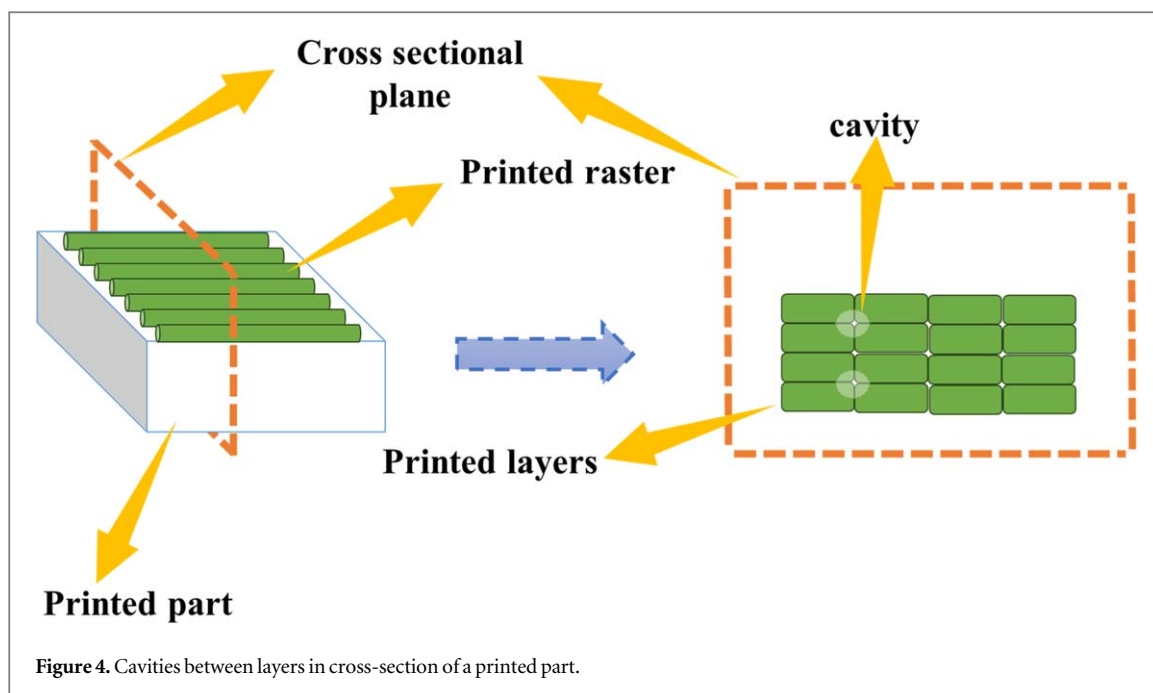
3. Results and discussion

3.1. Microstructure and printing quality

In extrusion-based 3D printing, the nozzle hole used to extrude the material is circular, resulting in cylindrical printed beads. When these beads are stacked and placed side by side to create the final printed object, gaps or spaces between the layers are commonly observed [40]. This is shown in figure 4, which depicts a cross-section of a printed part. The size of these gaps, which are known as inter-voids in some resources, is related to the quality of the printing process. If the print parameters and printability are favorable, the size of the spaces between the layers will decrease, resulting in a more uniform microstructure of the printed part [41]. Better overlap, material flow, and wettability lead to smaller cavities, improving the mechanical properties [42]. The presence of these gaps or cavities can contribute to damage propagation within the printed samples. Stress concentrations can occur at the layer interfaces, worsening crack growth or delamination [43]. These defects, combined with external loading or environmental factors, can compromise the structural integrity of the printed object and potentially cause failure or reduced performance over time.

The size of these cavities can be reduced through various approaches. One approach is post-processing, where additional treatments are applied after printing. For instance, Wang *et al* [44] used heat treatment to decrease the size of pores in continuous carbon fiber-reinforced composites (CCFRC), resulting in improved mechanical properties. Another method involves adjusting the printing parameters to minimize these empty spaces [45]. Printing parameters play a critical role in ensuring the quality of the print and the structural integrity of the final object. Figure 5(a) in this study illustrates the poorest printed sample in terms of printing parameters and mechanical properties (Sample #4: Printed under experimental conditions: printing speed: 6 mm s^{-1}, temperature: 180 °C, nozzle diameter: 0.6 mm). In this figure, the printed beads are widely spaced and disjointed. The cavities between the layers are large in size and numerous in quantity. These empty spaces significantly compromise the mechanical properties of the printed object as they provide favorable locations for delamination and crack initiation. Furthermore, the interlayer bonding is exceptionally weak in this sample, making it prone to easy detachment between the layers.

Figure 5(b) represents the best sample in terms of mechanical properties (Sample #3: Printed under experimental conditions: printing speed: 10 mm s^{-1}, temperature: 210 °C, nozzle diameter: 0.4 mm), observed through SEM imaging of its cross-section. The SEM image reveals a cohesive fusion of the printed elastomer's layers and beads, resulting in a consistent and uninterrupted structure. This suggests successful material flow during the printing process, indicating the absence of delamination or layer failure. Moreover, only a few small cavities are observed, demonstrating a high degree of integration and uniformity in the microstructure. The well-bonded layers contribute to the outstanding mechanical properties.

Figure 5. Comparing Printing Quality and Microstructural Integrity: worst (a) and (b) best-printed Samples.

3.2. Mechanical properties

Figure 6 and table 5 display the mechanical properties of the printed samples used in the context of Taguchi method analysis. The figure shows the ultimate tensile strength (UTS), Young's modulus (E), and Elongation at break (El %) for each sample.
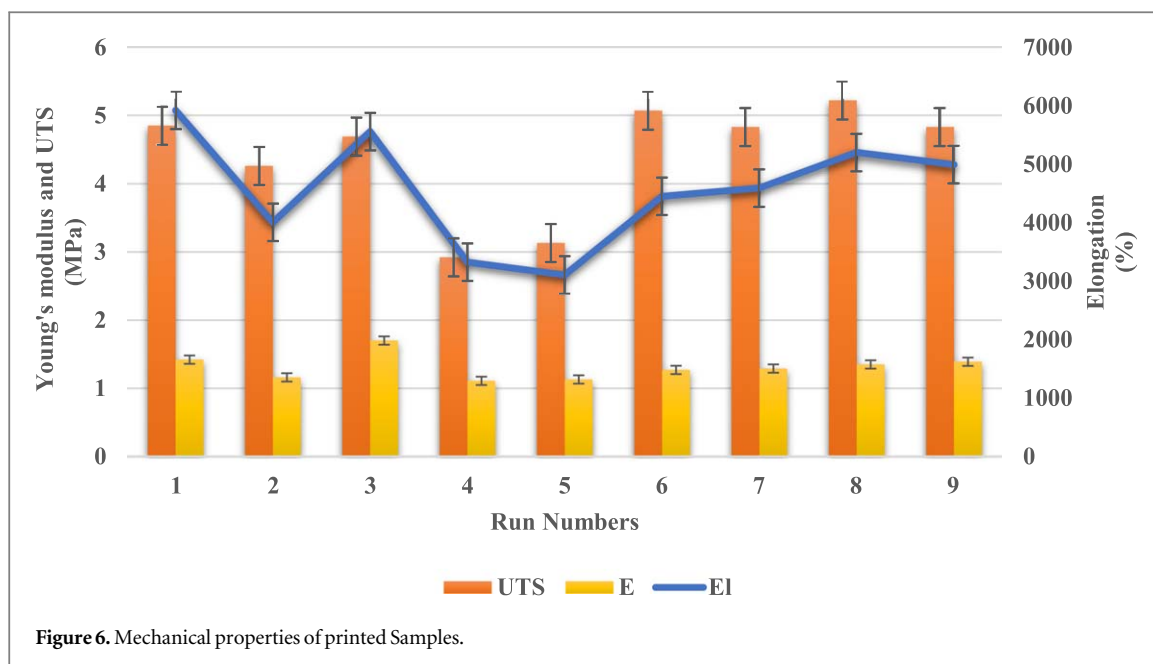
Figure 6. Mechanical properties of printed Samples.

Table 5. Inputs variables and the results of the present study.

Number of runs	Taguchi design	UTS (MPa)	El (%)	E (MPa)
1	0.4-180-2	4.85	5921.3	1.42
2	0.4-195-6	4.26	4006.1	1.16
3	0.4-210-10	4.69	5557.7	1.70
4	0.6-180-6	2.92	3324.49	1.11
5	0.6-195-10	3.13	3105.7	1.13
6	0.6-210-2	5.07	4450.9	1.27
7	0.8-180-10	4.83	4591.6	1.29
8	0.8-195-2	5.22	5199.0	1.35
9	0.8-210-6	4.83	4993.4	1.39

Table 6. Inputs variables for UTS in detail.

Number of samples	UTS (MPa)			Mean value	squared differences from the mean			Sample variance	Standard deviation	Error bar
	Test 1	Test 2	Test 3		Test 1	Test 2	Test 3			
1	4.86	4.9	4.79	4.85	0.0001	0.0025	0.0036	0.0021	0.0265	±0.0265
2	4.255	4.215	4.31	4.26	0.000025	0.002025	0.0025	0.002275	0.0477	±0.0275
3	4.68	4.66	4.73	4.69	0.0001	0.0009	0.0016	0.0013	0.036	±0.021
4	2.891	2.97	2.899	2.92	0.000841	0.0025	0.000441	0.001891	0.0435	±0.0251
5	3.11	3.185	3.095	3.13	0.0004	0.003025	0.001225	0.002325	0.0482	±0.0278
6	5.1	5.15	4.96	5.07	0.0009	0.0064	0.0121	0.0097	0.0985	±0.0569
7	4.78	4.86	4.85	4.83	0.0025	0.0009	0.0004	0.0019	0.0436	±0.0252
8	5.18	5.25	2.23	5.22	0.0016	0.0009	0.0001	0.0013	0.036	±0.021
9	4.805	4.86	4.825	4.83	0.000625	0.0009	0.000025	0.000775	0.0278	±0.0160

The corresponding printing parameters for each sample are also presented in table 5. Detailed tests are also presented in tables 6 and 7.

It is important to mention that by precisely controlling the printing parameters, printed TPEs can achieve significant stretchability, reaching up to 5921.3% which is the highest elongation at break compared to previous studies (table 8). These high stretchabilities have proven to be highly advantageous in various emerging fields, such as batteries [46], dielectric materials [47], and electronic skins [48]. Moreover, achieving a tensile strength (UTS) of 5.22 MPa and a Young modulus of 1.7 MPa is possible. However, it is crucial to note that these

Table 7. Inputs variables for E in detail.

Number of samples	E (MPa)			Mean value	squared differences from the mean			Sample variance	Standard deviation	Error bar
	Test 1	Test 2	Test 3		Test 1	Test 2	Test 3			
1	1.405	1.44	1.435	1.42	0.000471	0.000177	0.000069	0.0003585	0.0189	±0.0109
2	1.05	1.2	1.23	1.16	0.0121	0.0016	0.0049	0.0093	0.096	±0.056
3	1.675	1.705	1.72	1.7	0.000625	0.000025	0.0004	0.000525	0.0229	±0.0132
4	1.08	1.156	1.094	1.11	0.0009	0.002116	0.000256	0.001636	0.0405	±0.0234
5	1.108	1.126	1.156	1.13	0.000484	0.000016	0.000676	0.000588	0.0242	±0.0140
6	1.256	1.27	1.248	1.27	0.000004	0.000144	0.000100	0.000124	0.0111	±0.0064
7	1.307	1.276	1.287	1.29	0.000289	0.000196	0.000009	0.000247	0.0157	±0.0091
8	1.35	1.343	1.367	1.35	0.000011	0.000106	0.000188	0.0001525	0.0124	±0.0072
9	1.406	1.378	1.377	1.39	0.000361	0.000081	0.000100	0.000271	0.0165	±0.0095

Table 8. Previous studies on highly stretchable printed materials.

Reference	Printing method	Material	Elongation
[49]	Screw-based direct FDM	TPU	750%
[50]	DIW	silicone	2000%
[51]	Screw-based direct FDM	silicone	1859%
[52]	DIW	silicone	1260%
[53]	Pneumatic direct FDM	PBAT	1379%
[54]	Stereolithography	PU-PDMS-OH-HEMA	1046%
[55]	Pneumatic direct FDM	EVA	1000%
[56]	Filament-based FDM	TPU	702%
[57]	Filament-based FDM	PCL based TPU	720%
[58]	Filament-based FDM	PCL	1000%
[59]	Vat photopolymerization	fluorinated photocurable resin	523%
[60]	DIW	supramolecular ionogels	2500%
[61]	Solvent cast	SEBS	2200%
This study	Pneumatic direct FDM	Vistamaxx	5921.3%

properties cannot be simultaneously achieved and are dependent on the application. Furthermore, the mechanical properties are influenced by the combination of printing parameters. Therefore, it is necessary to analyze the role of the intersection effect of related parameters and in what amount it is (interaction terms) to determine the optimal printing parameters. Nevertheless, specific general trends can be observed in figure 6.

Samples 1 and 5 demonstrate the maximum and minimum elongation at break, respectively. Sample 1 was printed at a speed of 2 mm s^{-1}, temperature of 180 (°C), and nozzle diameter of 0.4 mm; while Sample 5 was printed at a speed of 10 mm s^{-1}, temperature of 195 (°C), and nozzle diameter of 0.6 mm. Therefore, higher printing speeds can be associated with decreased elongation at break in this case. This can be attributed to several factors. Firstly, slower printing speed ensures the material extruded from the nozzle is continuous and without breaking. The slower printing speed also produces a better surface finish [62]. Secondly, rapid printing speeds can introduce increased mechanical stresses on the printed material. Quick movements and abrupt accelerations/decelerations can induce internal stresses and generate defects within the printed object. These defects can act as stress concentration points, reducing the overall elongation capability and increasing the likelihood of failure at lower strain levels. Some defects caused by high printing speeds can be seen in the final printed parts. One example is shown in figure 7(a), where the visual defect occurred due to the acceleration and deceleration of the nozzle in the middle of the sample. Another reason for reduced mechanical properties is improper material flow at high speeds or other unfavorable combinations of printing parameters. Poor material flow can lead to rounded cross-sections and spaced-out beads with large gaps between them, as illustrated in figure 7(b). In contrast, good material flow results in better connections between beads and an oval cross-section of the beads, as shown in figure 7(c).

Sample 8 (0.8-195-2) demonstrates the highest UTS: 5.22 MPa among all the samples and sample 4 (0.6-180-6) shows the lowest amount of UTS: 2.92MPa. The key distinction between Sample 8 and Sample 4 lies in the lower printing speed used, which resulted in an increased UTS, modulus, and elongation. Consequently, lower printing speeds similarly affect UTS, modulus, and elongation.

Sample 1 (0.4-180-2) exhibits the highest modulus: 1.42 MPa compared to all the other samples. The key distinguishing factor between sample 1 and sample 4 (0.6-180-6) with the lowest E: 1.11 MPa is the nozzle
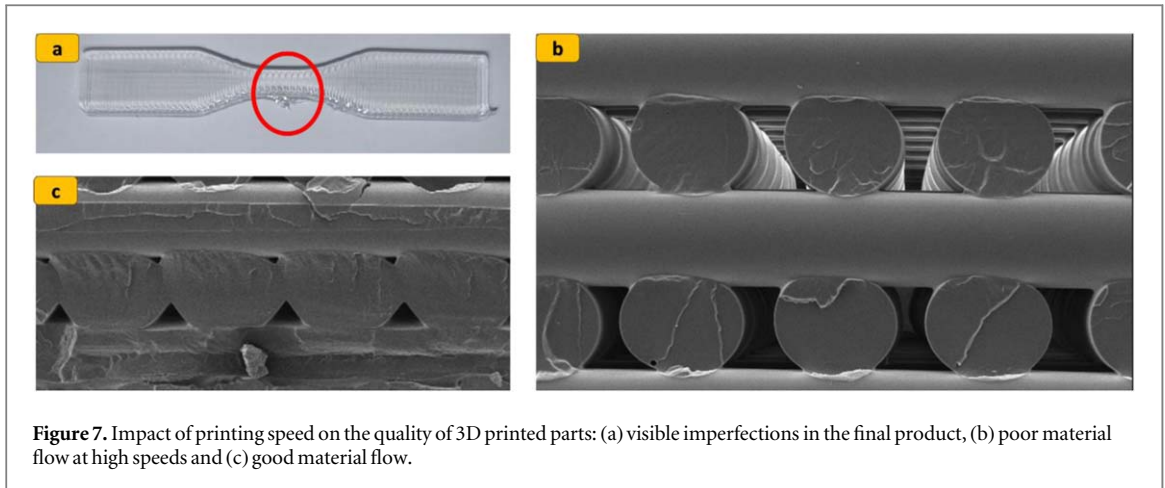
Figure 7. Impact of printing speed on the quality of 3D printed parts: (a) visible imperfections in the final product, (b) poor material flow at high speeds and (c) good material flow.

diameter and the printing speed. In sample 1, the nozzle diameter was set to 0.4 mm, whereas in sample 4, it was set to 0.6 mm. Moreover, as concluded previously increasing the printing speed also deteriorates the properties.

A higher nozzle temperature generally improves the adhesion and fusion between printed layers, resulting in enhanced interlayer strength and overall mechanical performance. It promotes better cohesion between the layers, ensuring a sturdy structure [40]. These findings were obtained through prior investigations. Coogan *et al* [63] conducted a study on the bonding characteristics of extruded filaments. They printed hollow boxes with a one-raster thickness, which were later cut into test specimens using a laser cutter. The study revealed that higher extrusion temperatures led to significantly stronger bonds due to increased wetting. At elevated temperatures, the molten PLA exhibited enhanced fluidity, allowing for improved adhesion between the newly deposited PLA fiber and the previously extruded filament. Consequently, this increased the bond width between the extruded rasters and subsequently resulted in enhanced strength.

However, it is notable that excessively high nozzle temperatures can lead to adverse effects, such as deformation, warping, and reduced dimensional accuracy of the printed object. Guessasma *et al* [64] conducted a study focusing on the influence of printing temperature on PLA-PHA plastic. The findings indicated that as the temperature rose to 240 °C, both the tensile strength and strain at break exhibited an increase. However, beyond a temperature of 250 °C, the mechanical properties of the material began to deteriorate.

Conversely, lower nozzle temperatures can result in diminished layer adhesion and weaker bonding between layers. This weakens the overall mechanical strength of the printed part. The layers may not firmly hold together, affecting the structural integrity.

3.3. S/N ratio analysis

The signal-to-noise ratio measures how the response varies relative to the nominal or target value under different noise conditions. In this study for all responses the quality characteristic of 'the-larger-the-better' is applied for the mean square deviation (MSD) and the S/N ratio analysis, equation (1).

$$\frac{S}{N} = -10 \left[\frac{1}{n} \sum_{i=1}^{n} \frac{1}{y_i^2} \right] \tag{1}$$

In this equation, y_i is the desired output (here it can be UTS, E, and El) and n is the number of experiments. This equation is used for finding the optimized set of parameters.

The main effects plot which shows how each factor affects the response characteristic (S/N ratio, means, slopes, standard deviations) is illustrated in figure 8 for all responses. It should be noted here that a main effect exists when different levels of a factor affect the characteristic differently [65–67].

For the ultimate tensile strength, as shown in figure 8(a), the S/N ratio increases with an increase in extrusion temperature, reaching its maximum when the temperature is set at the highest level (level 3). When the nozzle diameter is at its highest level (level 3), the highest UTS is achieved. By decreasing the nozzle diameter, the UTS first decreases, hitting the lowest point at level 2, and then increases.

Regarding printing velocity, the best UTS is achieved when the velocity is at its lowest level (level 1). It is also worth noting that with an increase in print speed, the S/N ratio response first decreases and then slightly increases.

The optimum combination for the highest UTS is $A_3B_3C_1$ (nozzle diameter at the third level, extrusion temperature at the third level, and printing velocity at the first level). In addition, the significance of parameters
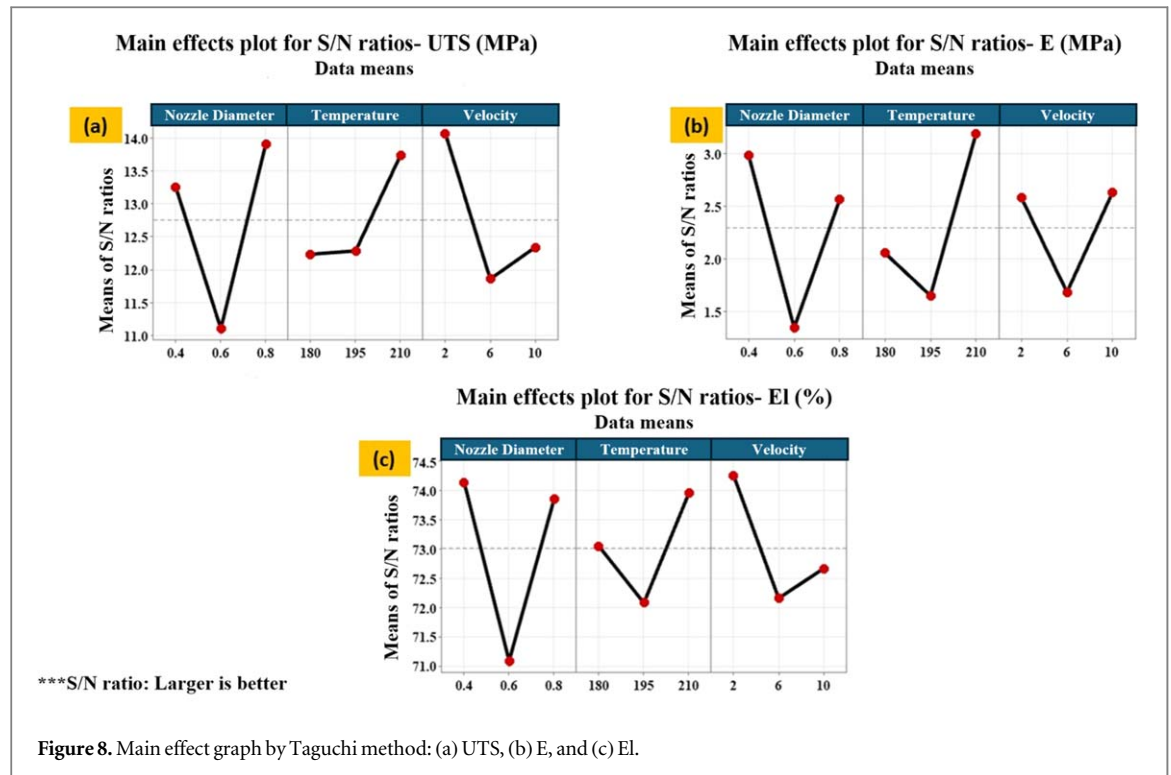
Figure 8. Main effect graph by Taguchi method: (a) UTS, (b) E, and (c) El.

without considering their interaction effects is A > C > B. This means that the effect of nozzle diameter on the UTS is higher than that of printing velocity, and the temperature effect is the lowest.

For Young's modulus, as shown in figure 8(b), the highest E is obtained when the nozzle diameter is at its lowest level (level 1). As the nozzle diameter increases, Young's modulus first decreases to its lowest point and then increases again. Considering the temperature impact, the highest E is obtained at the highest level of extrusion temperature (level 3), while the lowest E is recorded at the second temperature level (level 2). The worst result for Young's modulus is observed when the printing velocity is at its second level, and the best result is obtained when it is at its third level, which is negligibly higher than that of the first level. The best combination for Young's modulus is $A_1B_3C_3$. The significance of the parameters is A > B > C.

The main effects plot for elongation is shown in figure 8(c). Based on this figure, the nozzle diameter and printing velocity exhibit similar trends. The highest elongation occurs when the nozzle diameter and velocity are set at their first levels. As these levels increase, elongation initially decreases to its lowest point at level 2, then increases again. In contrast, temperature yields the best results at its highest level (level 3), with the worst elongation occurring at the second level (level 2). The optimal combination is $A_1B_3C_1$, with parameter significance ranking as A > C > B.

Figures 9 to 11 display contour plots for UTS, E, and El.

Based on figure 9(a), when velocity is kept constant at 6 mm s^{-1}, the interaction effect between nozzle diameter and temperature on UTS shows that the highest UTS is achieved when the nozzle diameter is 0.4 mm and the temperature is at its maximum (210 °C). The figure indicates that as temperature increases, UTS also increases. This finding about the impact of printing temperature is consistent with previous research by Hsueh *et al* [68]. In their study, they investigated the effects of temperature and printing speed on the FDM process for PETG. They discovered that increasing the printing temperature significantly improves the material's tensile strength, compressive strength, and flexural strength. In figure 9(b), (a) combination effect of velocity and temperature on UTS is shown while the nozzle diameter is held constant at 0.6 mm. It is evident that as velocity increases, UTS decreases, with the highest UTS achieved at velocities less than 3 mm s^{-1}. Figure 9(c) demonstrates the interaction effect of velocity and nozzle diameter on UTS, with temperature constant at 195 °C. The highest UTS is obtained when both nozzle diameter and velocity are at their lowest levels.

Figure 10(a) illustrates the interaction effect of nozzle diameter and temperature on E, with velocity constant at the second level (velocity = 6 mm s^{-1}). According to this figure, increasing temperature and nozzle diameter positively impact the amount of E. The highest amount of E is achieved when the nozzle diameter is 0.4 mm and the temperature is 210 °C. In figure 10(b), the combined effect of velocity and temperature on E is shown, with the nozzle diameter set at the second level. The figure indicates that increasing velocity hurts the amount of E, and the highest E is achieved when the nozzle diameter is 0.4 mm and the temperature is 195 °C. Figure 10(c) presents a contour plot of the interaction effect of velocity and nozzle diameter on the amount of E. It reveals that

Figure 9. Contour plots for the UTS: (a) nozzle diameter versus temperature while keeping velocity constant at 6 mm s^{-1}, (b) velocity versus temperature while keeping nozzle diameter constant at 0.6 mm, and (c) velocity versus nozzle diameter while keeping the temperature constant at 195 ($^{\circ}$C).

Figure 10. Contour plots for the E: (a) nozzle diameter versus temperature while keeping velocity constant at 6 mm s^{-1}, (b) velocity versus temperature while keeping nozzle diameter constant at 0.6 mm, and (c) velocity versus nozzle diameter while keeping the temperature constant at 195 ($^{\circ}$C).
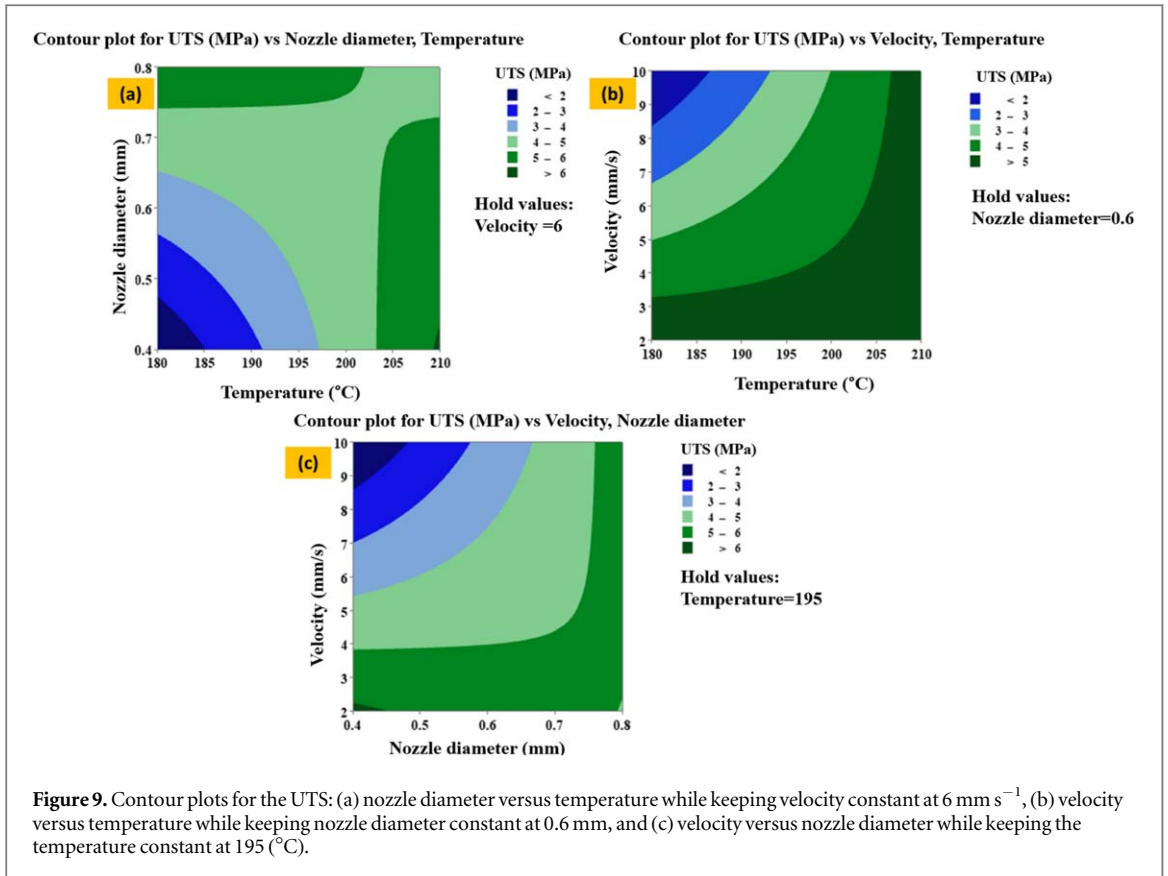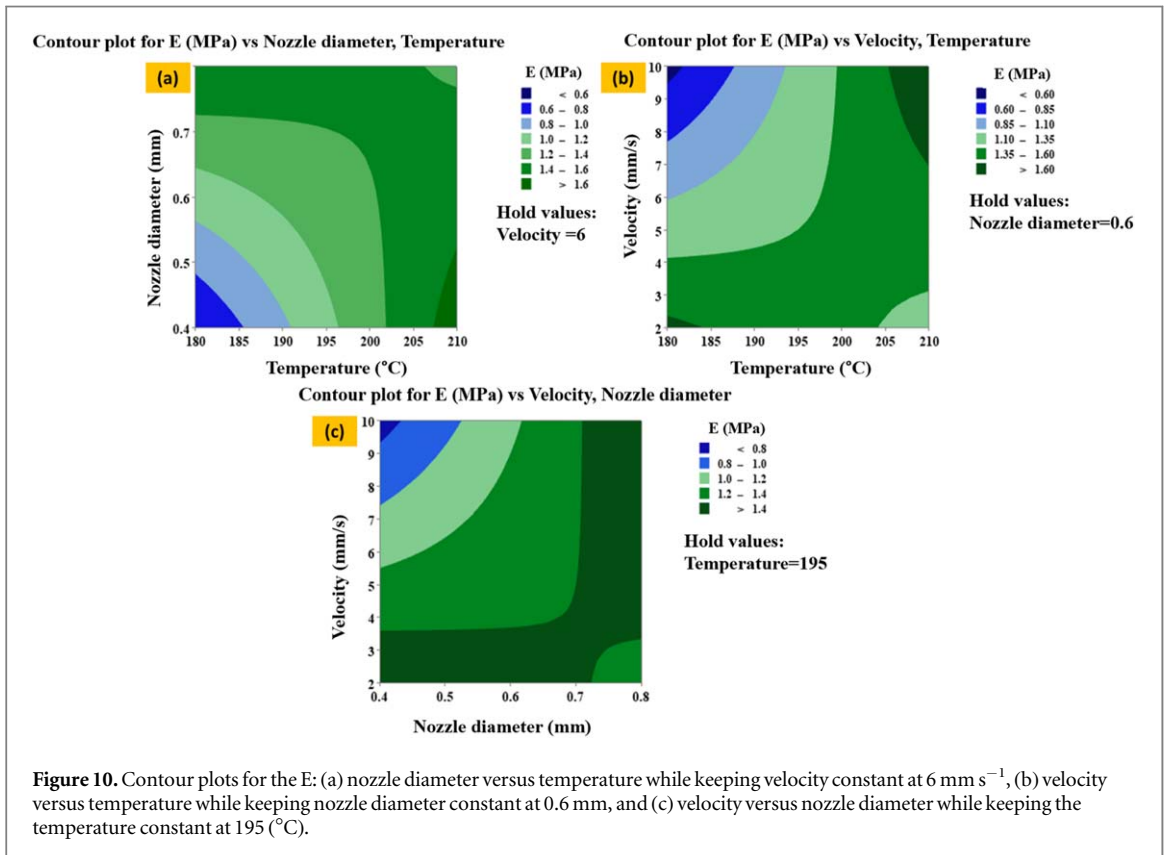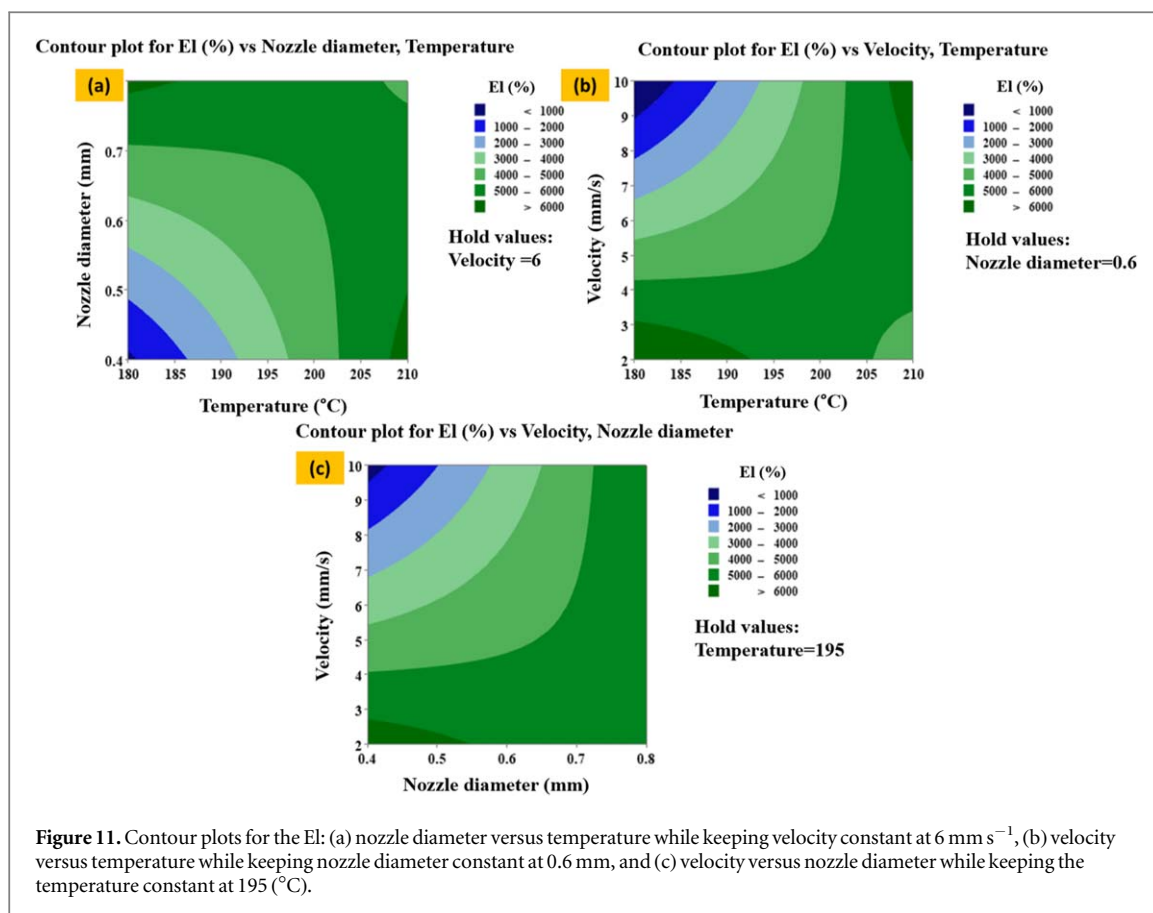
Figure 11. Contour plots for the El: (a) nozzle diameter versus temperature while keeping velocity constant at 6 mm s^{-1}, (b) velocity versus temperature while keeping nozzle diameter constant at 0.6 mm, and (c) velocity versus nozzle diameter while keeping the temperature constant at 195 ($^{\circ}$C).

the highest E is obtained at a velocity of 2–4 mm s^{-1} and a nozzle diameter of 0.4–0.7 mm. Increasing velocity and nozzle diameter hurt E.

The interaction effect of nozzle diameter and temperature on El is shown in figure 11(a). Based on this figure, increasing each parameter of nozzle diameter and temperature at a constant velocity of 6 mm s^{-1} has a positive impact on El. By increasing the temperature or nozzle diameter, the El amount increases. Previous research by Karimi *et al* [53] has also found that the nozzle temperature plays a significant role in the printing process. In their study, they observed that when all other parameters are kept constant, the printed Polybutylene Adipate-co-Terephthalate (PBAT) exhibited the best elongation at break when the nozzle temperature was at its highest setting.

Based on figure 11, The highest El is achieved when the temperature is 195 $^{\circ}$C and the nozzle diameter is 0.8 mm, or when the temperature is 210 $^{\circ}$C and the nozzle diameter is 0.4 mm. By keeping the nozzle diameter constant at 0.6 mm, the contour plot showing the interaction effect of temperature and velocity on El is obtained, as shown in figure 11(b). According to this figure, increasing the velocity has a negative impact on the El amount. The combination for the highest El is when the velocity is at its lowest level and the temperature is between 180 $^{\circ}$C and 190 $^{\circ}$C. In figure 11(c), the interaction effect of nozzle diameter and velocity on El is shown, with the temperature kept at its second level. The highest amount of El is obtained when the nozzle diameter and velocity are at their lowest levels. Increasing the nozzle diameter and velocity results in a decrease in the El amount.

Wang *et al* [69] conducted a study on the impact of different printing parameters, such as nozzle temperature, platform temperature, printing speed, and layer thickness, on the mechanical properties and microstructure of carbon fiber (CF) and glass fiber (GF) reinforced PEEK composite. The authors concluded that an increase in printing speed negatively affects all mechanical properties of printed fiber-reinforced PEEK composites. Moreover, a lower printing speed has the potential to enhance printing stability and facilitate the extrusion and adhesion of high-viscosity PEEK composites.

3.4. ANOVA analysis

The purpose of the analysis of variance is to investigate which parameters significantly impact the resultant characteristic and their relative influence. This analysis is conducted at a 95% confidence interval level. To determine the importance and significance of each parameter, the F value and P value given in the ANOVA table

Table 9. ANOVA results for the UTS.

Factor	UTS					
	S	R-sq	R-sq(adj)	R-sq(pred)		
	0.648373	84.98%	39.90%	0.00%		
	DOF	SS	MS	F-value	P-value	Contribution percentage
Nozzle Diameter	1	2.4179	0.7926	5.75	0.139	34.13%
Temperature	1	2.2760	2.4179	5.41	0.145	29.07%
Velocity	1	2.1408	2.2760	5.09	0.153	36.80%
Nozzle Diameter*Temperature	1	2.5210	2.1408	6.00	0.134	
Nozzle Diameter*Velocity	1	2.2172	2.5210	5.27	0.148	
Temperature*Velocity	1	1.7122	2.2172	4.07	0.181	
Error	2	0.8408				
Total	8	5.5962				100%

Table 10. ANOVA results for the E.

Factor	E					
	S	R-sq	R-sq(adj)	R-sq(pred)		
	0.0325869	99.21%	96.84%	51.04%		
	df	SS	MS	F-value	P-value	Contribution percentage
Nozzle Diameter	1	0.266876	0.123754	116.54	0.008	36.94%
Temperature	1	0.123754	0.060812	57.27	0.017	32.43%
Velocity	1	0.060812	0.193503	182.22	0.005	30.63%
Nozzle Diameter*Temperature	1	0.193503	0.125952	118.61	0.008	
Nozzle Diameter*Velocity	1	0.125952	0.084152	79.25	0.012	
Temperature*Velocity	1	0.084152	0.198860	187.27	0.005	
Error	2	0.198860	0.001062			
Total	8	0.002124				100%

Table 11. ANOVA results for the El.

Factor	El					
	S	R-sq	R-sq(adj)	R-sq(pred)		
	416.751	95.31%	81.24%	0.00%		
	df	SS	MS	F-value	P-value	Contribution percentage
Nozzle Diameter	1	3295125	3295125	18.97	0.049	21.9%
Temperature	1	1470384	1470384	8.47	0.101	45.67%
Velocity	1	5941600	5941600	34.21	0.028	32.43%
Nozzle Diameter*Temperature	1	3459509	3459509	19.92	0.047	
Nozzle Diameter*Velocity	1	3397573	3397573	19.56	0.048	
Temperature*Velocity	1	5676420	5676420	32.68	0.029	
Error	2	347364	173682		0.049	
Total	8	7404530				100%

are utilized. If the P value is less than 0.05, the significance of the related term is established. A fitted regression model is also created for the three responses. Tables 9–11 consists of the results of ANOVA analysis, where:

S: represents the standard deviation of the distance between the data and the fitted values.

R-sq: R^2 is the percentage of variation in the response explained by the model.

R-sq (adj): is

DOF is the degree of freedom, SS is the sum of squares, and MS is: the mean sum of squares.

For the UTS, none of the P-values are less than 0.05 indicating that none of the factors are significant. For the Young's modulus, however, all P-values are less than 0.05, confirming that all factors are significant. For the elongation, all values except the temperate are significant.

Table 12. Actual results obtained from additional tests versus predicted results from the regression models.

Confirmation tests set	Fitted value by the model			The actual		
	UTS	E	El	UTS	E	El
0.6-195-6	4.2222	1.31333	4572.24	4.73	1.22	4224.9
Error	10.73%	7.65%	8.22%			
0.8-180-10	4.67413	1.28714	4486.62	4.83	1.29	4591.6
Error	3.22%	6.75%	2.29%			

Regression models for the UTS, E, and El are given below.

$$UTS(MPa) = -37.0 + 89.1\,A + 0.241\,B - 5.26\,C - 0.490\,A_*B$$
$$+ 1.723\,A_*C + 0.0202\,B_*C$$

$$E(MPa) = -5.425 + 20.17\,A + 0.03938\,B - 1.581\,C - 0.1095\,A_*B$$
$$+ 0.3357\,A_*C + 0.006881\,B_*C$$

$$El\% = -26597 + 104062\,A + 193.6\,B - 8760\,C - 574\,A_*B$$
$$+ 2133\,A_*C + 36.76\,B_*C$$

3.5. Confirmation test

The confirmation step is the final step in authenticating the results achieved from the previous analysis phase. Confirmation tests aim to verify the regression model provided by the ANOVA analysis with the experimental results to determine whether the model can predict the results accurately or not.

To evaluate the current study's regression model, two additional tests were conducted, and their results were compared to the values predicted by the regression model. The results and the error percentage of the regression model are provided in table 12.

In this table, the fitted values are predicted by the regression model, while the actual values are those obtained from the experiments.

As it is clear from the table, regression models could effectively predict the results by a maximum of 10% error.

4. Conclusion

In this study, a pneumatic-based direct pellet printing method with a propylene-based thermoplastic elastomer (Vistamaxx™ 6202) was evaluated to directly print very soft and stretchable parts from granules. The main goal of the study was to optimize the printing parameters and examine how they affected the mechanical properties of the printed elastomers. The Taguchi method was employed as a statistical approach to design experiments, create a model of the system, and optimize the responses. This approach allowed for efficiently determining the optimal printing parameters that would maximize the desired properties. The printing parameters investigated in this study included the nozzle temperature (180 °C, 195 °C, 210 °C), nozzle diameter (0.4 mm, 0.6 mm, 0.8 mm), and printing speed (2 mm.s^{-1}, 6 mm.s^{-1}, 10 mm.s^{-1}). Tensile tests were conducted to evaluate the mechanical properties of the printed elastomers, including stretchability, Young's modulus, and tensile strength. Dog bone-shaped specimens with consistent and variable printing parameters were tested, strain-stress curves were recorded, and the average values from multiple specimens were calculated. Scanning electron microscopy (SEM) was used to examine the interlayer adhesion and structural integrity of the printed samples, and analyze fracture cross-sections to assess the bonding between layers.

The SEM analysis demonstrated satisfactory interlayer adhesion and structural integrity of the printed samples, indicating a strong bond between the layers. By accurately managing the printing parameters, notable stretchability in the printed TPEs was achieved, with the ability to reach up to 5921.3% elongation. It is feasible to attain a tensile strength (UTS) of 5.22 MPa and Young's modulus of 1.7 MPa.

Main effect plots and interaction plots were also obtained from the Taguchi analysis to help interpret the data. The regression model demonstrated sufficient predictive capability, with minimal deviation between the predicted and actual data.

The results show that optimizing printing parameters can lead to improved stretchability and mechanical properties. However, there are limitations to this technique. One limitation is the small capacity of the printer's cylinder or container, which can hinder its application to small parts and prevent continuous printing.

Additionally, storing material in the container for extended periods can cause thermal degradation of the material.

Despite these limitations, this innovative approach can be applied to other thermoplastic elastomers, enabling the printing of a wide range of elastomers and soft materials that are difficult to print using filament-based techniques. This technique has potential applications in cutting-edge fields such as wearable devices, soft robotics, stretchable sensors and actuators, and soft biomedical devices.

Data availability statement

All data that support the findings of this study are included within the article (and any supplementary files).

Appendix

Table A1. ANOVA table for UTS.

Source	Sum of Squares	df	Mean Square	F-value	p-value	
Model	11.98	12	0.9979	1.247E+06	<0.0001	significant
A-Nozzle Diameter	0.1105	1	0.1105	1.381E+05	<0.0001	
B-Printing Speed	3.14	1	3.14	3.919E+06	<0.0001	
C-Nozzle Temperature	1.01	1	1.01	1.260E+06	<0.0001	
AB	0.0001	1	0.0001	166.67	0.0002	
AC	0.0625	1	0.0625	78125.00	<0.0001	
BC	0.0030	1	0.0030	3781.25	<0.0001	
A^2	0.0368	1	0.0368	46020.83	<0.0001	
B^2	0.3051	1	0.3051	3.814E+05	<0.0001	
C^2	0.4732	1	0.4732	5.915E+05	<0.0001	
ABC	0.0000	0				
A^2B	0.0133	1	0.0133	16666.67	<0.0001	
A^2C	0.4380	1	0.4380	5.475E+05	<0.0001	
AB^2	0.0029	1	0.0029	3681.82	<0.0001	
AC^2	0.0000	0				
B^2C	0.0000	0				
BC^2	0.0000	0				
A^3	0.0000	0				
B^3	0.0000	0				
C^3	0.0000	0				
Pure Error	3.200E-06	4	8.000E-07			
Cor Total	11.98	16				

Table A2. ANOVA table for El.

Source	Sum of Squares	df	Mean Square	F-value	p-value	
Model	1.298E+07	9	1.442E+06	10.09	0.0030	significant
A-Nozzle Diameter	3.430E+05	1	3.430E+05	2.40	0.1653	
B-Printing Speed	3.482E+06	1	3.482E+06	24.36	0.0017	
C-Nozzle Temperature	9.677E+05	1	9.677E+05	6.77	0.0353	
AB	23755.48	1	23755.48	0.1662	0.6957	
AC	33874.40	1	33874.40	0.2370	0.6412	
BC	4.333E+05	1	4.333E+05	3.03	0.1252	
A^2	6.912E+05	1	6.912E+05	4.84	0.0638	
B^2	6.542E+05	1	6.542E+05	4.58	0.0697	
C^2	1.511E+06	1	1.511E+06	10.57	0.0140	
Residual	1.000E+06	7	1.429E+05			
Lack of Fit	1.000E+06	3	3.335E+05			
Pure Error	0.0000	4	0.0000			
Cor Total	1.398E+07	16				

Table A3. ANOVA table for E.

Source	Sum of Squares	df	Mean Square	F-value	p-value	
Model	0.4581	9	0.0509	19.90	0.0003	significant
A-Nozzle Diameter	0.0310	1	0.0310	12.11	0.0103	
B-Printing Speed	0.0509	1	0.0509	19.91	0.0029	
C-Nozzle Temperature	0.1159	1	0.1159	45.31	0.0003	
AB	0.0138	1	0.0138	5.38	0.0535	
AC	0.0036	1	0.0036	1.41	0.2742	
BC	0.0696	1	0.0696	27.21	0.0012	
A^2	0.0007	1	0.0007	0.2754	0.6160	
B^2	0.0206	1	0.0206	8.04	0.0252	
C^2	0.1094	1	0.1094	42.79	0.0003	
Residual	0.0179	7	0.0026			
Lack of Fit	0.0179	3	0.0060			
Pure Error	0.0000	4	0.0000			
Cor Total	0.4760	16				

ORCID iDs

Abbas Bayati ⬤ https://orcid.org/0009-0007-2740-7213
Davood Rahmatabadi ⬤ https://orcid.org/0000-0002-6898-3061
Majid Baniassadi ⬤ https://orcid.org/0000-0002-4434-082X
Ali Zolfagharian ⬤ https://orcid.org/0000-0001-5302-360X
Mahdi Bodaghi ⬤ https://orcid.org/0000-0002-0707-944X
Mostafa Baghani ⬤ https://orcid.org/0000-0001-6695-3128

References

[1] Gyu Son S *et al* 2023 Ultra-fast self-healable stretchable bio-based elastomer/graphene ink using fluid dynamics process for printed wearable sweat-monitoring sensor *Chem. Eng. J.* **454**

[2] Nie M, Wen L, Chen S, Ai L, Shen J, Zhao Y na, Yin K and Dou G 2022 Strain sensor with enhanced sensitivity for wearable electronics using an over-balanced planar elastomer *Macromol. Mater. Eng.* **307**

[3] Ritere A, Jurinovs M, Platnieks O, Barkane A and Gaidukovs S 2024 A super-tough plant oil based elastomer for UV-light assisted 3D printed soft robotics and shape-memory *J. Mater. Chem. A* **12** 16569–82

[4] Jiang C *et al* 2021 Self-healing polyurethane-elastomer with mechanical tunability for multiple biomedical applications in vivo *Nat. Commun.* **12** 1–13

[5] Parida K, Thangavel G, Cai G, Zhou X, Park S, Xiong J and Lee P S 2019 Extremely stretchable and self-healing conductor based on thermoplastic elastomer for all-three-dimensional printed triboelectric nanogenerator *Nat. Commun.* **10** 1–9

[6] Duduta M, Hajiesmaili E, Zhao H, Wood R J and Clarke D R 2019 Realizing the potential of dielectric elastomer artificial muscles *Proc. Natl. Acad. Sci. U. S. A.* **116** 2476–81

[7] Mirasadi K, Rahmatabadi D, Ghasemi I, Khodaei M, Baniassadi M and Baghani M 2024 Investigating the effect of ABS on the mechanical properties, morphology, printability, and 4D printing of PETG-ABS blends *Macromol. Mater. Eng.* **309** 2400038

[8] Wang Z, Xiang Y, Zhang S, Liu X, Ma J, Tan J and Wang L 2024 Physics-informed springback prediction of 3D aircraft tubes with six-axis free-bending manufacturing *Aerosp. Sci. Technol.* **147**

[9] He L, Chen B, Liu Q, Chen H, Li H, Chow W T, Tang J, Du Z, He Y and Pan J 2024 A quasi-exponential distribution of interfacial voids and its effect on the interlayer strength of 3D printed concrete *Addit. Manuf.* **89** 104296

[10] Rahmatabadi D, Soltanmohammadi K, Aberoumand M, Soleyman E, Ghasemi I, Baniassadi M, Abrinia K, Bodaghi M and Baghani M 2023 Development of pure poly vinyl chloride (PVC) with excellent 3D printability and macro- and micro-structural properties *Macromol. Mater. Eng.* **308** 2200568

[11] He L, Pan J, Hee Y S, Chen H, Li L G, Panda B and Chow W T 2024 Development of novel concave and convex trowels for higher interlayer strength of 3D printed cement paste *Case Stud. Constr. Mater.* **21** e03745

[12] Wang Z, Wang Z, Zheng Y, He Q, Wang Y and Cai S 2020 Three-dimensional printing of functionally graded liquid crystal elastomer *Sci. Adv.* **6**

[13] Wu Y and Chiu G 2021 An improved height difference based model of height profile for drop-on-demand 3D printing with UV curable Ink *Proc. of the American Control Conf.* 2021-May (https://doi.org/10.23919/ACC50511.2021.9483241)

[14] Herzberger J, Sirrine J M, Williams C B and Long T E 2019 Polymer design for 3D printing elastomers: recent advances in structure, properties, and printing *Prog. Polym. Sci.* **97** 101144

[15] Rahmatabadi D, Aberoumand M, Soltanmohammadi K, Soleyman E, Ghasemi I, Baniassadi M, Abrinia K, Bodaghi M and Baghani M 2023 Toughening PVC with biocompatible PCL softeners for supreme mechanical properties, morphology, shape memory effects, and FFF printability *Macromol. Mater. Eng.* **308** 2300114

[16] Gao Y C, Duan D X, Zeng S Y, Zheng H, Wang L P and Tan J R 2024 Programming time-dependent behavior in 4D printing by geometric and printing parameters *Adv. Manuf.* **12** 1–16

[17] Peng X, Han Y, Liu G, Li J, Yi B, Sa G and Jiang S 2024 Effect of manufacturing process parameters on the compression and energy absorption properties of 4D-printed deformable honeycomb structure *Smart Mater. Struct.* **33** 075035

[18] Lee C H, Padzil F N B M, Lee S H, Ainun Z M A and Abdullah L C 2021 Potential for natural fiber reinforcement in PLA polymer filaments for fused deposition modeling (FDM) additive manufacturing: a review *Polym.* **13** 1407

[19] Wu Y and Chiu G 2023 Error diffusion based feedforward height control for inkjet 3D printing *IEEE/ASME Int. Conf. on Advanced Intelligent Mechatronics* (AIM) 2023-June (https://doi.org/10.1109/AIM46323.2023.10196116)

[20] Xu J T, Zhang G W and Chen M M 2024 Optimizing mechanical properties of HIPS fabricated with low-cost desktop 3D printers: investigating the impact of process parameters *Adv. Manuf.* **12** 379–95

[21] Khondoker M A H and Sameoto D 2019 Direct coupling of fixed screw extruders using flexible heated hoses for FDM printing of extremely soft thermoplastic elastomers *Prog. Addit. Manuf.* **4** 197–209

[22] Costi L, Georgopoulou A, Mondal S, Iida F and Clemens F 2024 3D Printable Self-Sensing Magnetorheological Elastomer *Macromol. Mater. Eng.* **309**

[23] Singamneni S, Behera M P, Truong D, Le Guen M J, Macrae E and Pickering K 2021 Direct extrusion 3D printing for a softer PLA-based bio-polymer composite in pellet form *J. Mater. Res. Technol.* **15** 936–49

[24] Roels E, Terryn S, Iida F, Bosman A W, Norvez S, Clemens F, Van Assche G, Vanderborght B and Brancart J 2022 Processing of self-healing polymers for soft robotics *Adv. Mater.* **34** 2104798

[25] Fazli A and Rodrigue D 2020 Waste rubber recycling: a review on the evolution and properties of thermoplastic elastomers *Mater* **13** 782

[26] Aiswarya S, Awasthi P and Banerjee S S 2022 Self-healing thermoplastic elastomeric materials: challenges, opportunities and new approaches *Eur. Polym. J.* **181** 111658

[27] Awasthi P and Banerjee S S 2021 Fused deposition modeling of thermoplastic elastomeric materials: challenges and opportunities *Addit. Manuf.* **46** 102177

[28] Pawar A, Ausias G, Corre Y M, Grohens Y and Férec J 2022 Mastering the density of 3D printed thermoplastic elastomer foam structures with controlled temperature *Addit. Manuf.* **58** 103066

[29] Ma Y, Xin C, Huang G, Wang Y and He Y 2022 Fundamental influences of propylene-based elastomer on the foaming properties of high melt strength polypropylene based on extrusion foaming *Polym. Eng. Sci.* **62**

[30] Wang X, Hu S, Guo Y, Li G and Xu R 2019 Toughened high-flow polypropylene with polyolefin-based elastomers *Polym.* **11** 1976

[31] Cvek M, Kracalik M, Sedlacik M, Mrlik M and Sedlarik V 2019 Reprocessing of injection-molded magnetorheological elastomers based on TPE matrix *Composites* B **172** 253–61

[32] Tunçel O 2024 Optimization of charpy impact strength of tough PLA samples produced by 3D printing using the Taguchi Method *Polymers* **16** 459

[33] Kafshgar A R, Rostami S, Aliha M R M and Berto F 2021 Optimization of properties for 3D printed PLA material using Taguchi, ANOVA and multi-objective methodologies *Procedia Structural Integrity* **34**

[34] Tunçel O, Tüfekci K and Kahya Ç 2024 Multi-objective optimization of 3D printing process parameters using gray-based Taguchi for composite PLA parts *Polym. Compos.* **45** 12870–84

[35] Deng X, Zeng Z, Peng B, Yan S and Ke W 2018 Mechanical properties optimization of poly-ether-ether-ketone via fused deposition modeling *Materials* **11** 216

[36] Liu X, Zhang M, Li S, Si L, Peng J and Hu Y Mechanical property parametric appraisal of fused deposition modeling parts based on the gray Taguchi method **89** 2387–97

[37] Rahmatabadi D, Soltanmohammadi K, Pahlavani M, Aberoumand M, Soleyman E, Ghasemi I, Baniassadi M, Abrinia K, Bodaghi M and Baghani M 2023 Shape memory performance assessment of FDM 3D printed PLA-TPU composites by box-behnken response surface methodology *Int. J. Adv. Manuf. Technol.* **127** 935–50

[38] Bayati A, Rahmatabadi D, Ghasemi I, Khodaei M, Baniassadi M, Abrinia K and Baghani M 2024 3D printing super stretchable propylene-based elastomer *Mater. Lett.* **361** 136075

[39] Kiendl J and Gao C 2020 Controlling toughness and strength of FDM 3D-printed PLA components through the raster layup *Composites* B **180** 107562

[40] Syrlybayev D, Zharylkassyn B, Seisekulova A, Akhmetov M, Perveen A and Talamona D 2021 Optimisation of strength Properties of FDM printed parts—a critical review *Polym.* **13** 1587

[41] Gupta C, MB P, Shet N K, Ghosh A K, Bandyopadhyay S and Mukhopadhyay P 2020 Microstructure and mechanical performance examination of 3D printed acrylonitrile butadiene styrene thermoplastic parts *Polym. Eng. Sci.* **60** 2770–81

[42] Rahmatabadi D, Bayati A, Khajepour M, Mirasadi K, Ghasemi I, Baniassadi M, Abrinia K, Bodaghi M and Baghani M 2024 Poly (ethylene terephthalate) glycol/carbon black composites for 4D printing *Mater. Chem. Phys.* **325** 129737

[43] Rahmatabadi D *et al* 2024 Advancing sustainable shape memory polymers through 4D printing of polylactic acid-polybutylene adipate terephthalate blends *Eur. Polym. J.* **216** 113289

[44] Wang K, Long H, Chen Y, Baniassadi M, Rao Y and Peng Y 2021 Heat-treatment effects on dimensional stability and mechanical properties of 3D printed continuous carbon fiber-reinforced composites *Compos. Part A Appl. Sci. Manuf.* **147** 106460

[45] Sun X, Mazur M and Cheng C T 2023 A review of void reduction strategies in material extrusion-based additive manufacturing *Addit. Manuf.* **67** 103463

[46] Yan W *et al* 2021 Superstretchable, thermostable and ultrahigh-loading lithium–sulfur batteries based on nanostructural gel cathodes and gel electrolytes *Nano Energy* **80** 105510

[47] Pan C, Markvicka E J, Malakooti M H, Yan J, Hu L, Matyjaszewski K and Majidi C 2019 A liquid-metal–elastomer nanocomposite for stretchable dielectric materials *Adv. Mater.* **31**

[48] Liu C, Huang N, Xu F, Tong J, Chen Z, Gui X, Fu Y and Lao C 2018 3D printing technologies for flexible tactile sensors toward wearable electronics and electronic skin *Polymers* **10** 1–31

[49] Leng J, Wu J, Chen N, Xu X and Zhang J 2020 The development of a conical screw-based extrusion deposition system and its application in fused deposition modeling with thermoplastic polyurethane *Rapid Prototyp. J.* **26** 409–17

[50] Zhou L Y, Gao Q, Fu J Z, Chen Q Y, Zhu J P, Sun Y and He Y 2019 Multimaterial 3D printing of highly stretchable silicone elastomers *ACS Appl. Mater. Interfaces* **11** 23573–83

[51] Gharaie S, Zolfagharian A, Moghadam A A A, Shukur N, Bodaghi M, Mosadegh B and Kouzani A 2023 Direct 3D printing of a two-part silicone resin to fabricate highly stretchable structures *Prog. Addit. Manuf.* **8**

[52] Hamidi A and Tadesse Y 2020 3D printing of very soft elastomer and sacrificial carbohydrate glass/elastomer structures for robotic applications *Mater. Des.* **187** 108324

[53] Karimi A, Rahmatabadi D and Baghani M 2024 Direct pellet three-dimensional printing of polybutylene adipate-co-terephthalate for a greener future *Polym.* **16** 267

[54] Wang D, Wang R, Chen S, Gao J, Cai C, Zheng Y, Liu X, Qu B, Chen N and Zhuo D 2024 Low viscosity and highly flexible stereolithographic 3D printing resins for flexible sensors *Mater. Des.* **243** 113052

[55] Luo S and Zhang X 2023 High-quality 3D printing of ethylene vinyl acetate with direct pellet-based FDM for medical applications: mechanical analysis, energy absorption and recovery evaluation *J. Mech. Behav. Biomed. Mater.* **148** 106231

[56] Xiao J and Gao Y 2017 The manufacture of 3D printing of medical grade TPU *Prog. Addit. Manuf.* **2** 117–23

[57] Haryńska A, Kucinska-Lipka J, Sulowska A, Gubanska I, Kostrzewa M and Janik H 2019 Medical-grade PCL based polyurethane system for FDM 3D printing—characterization and fabrication *Mater.* **12** 887

[58] Haque A N M A and Naebe M 2023 Material extrusion of wool waste/polycaprolactone with improved tensile strength and biodegradation *Polym.* **15** 3439

[59] Song Q *et al* 2024 3D printed elastic fluoropolymer with high stretchability and enhanced chemical resistance for microfluidic applications *Addit. Manuf.* **81**

[60] Chen L and Guo M 2021 Supramolecular Ionogels Integrated with Three-Dimensional Printable, Adhesive, Healable, and Recyclable Character *ACS Appl. Mater. Interfaces* **13** 25365–73

[61] Kumar A, Pandey P M, Jha S and Banerjee S S 2023 Experimental investigations into additive manufacturing of styrene-ethylene-butylene-styrene block copolymers using solvent cast 3D printing technique *Rapid Prototyp. J.* **29** 1367–85

[62] Kumaresan R, Samykano M, Kadirgama K, Ramasamy D, Keng N W and Pandey A K 2021 3D printing technology for thermal application: a brief review *J. Adv. Res. Fluid Mech. Therm. Sci.* **83** 84–97

[63] Coogan T J and Kazmer D O 2017 Bond and part strength in fused deposition modeling *Rapid Prototyp. J.* **23** 414–22

[64] Guessasma S, Belhabib S and Nouri H 2020 Thermal cycling, microstructure and tensile performance of PLA-PHA polymer printed using fused deposition modelling technique *Rapid Prototyp. J.* **26** 122–33

[65] Hasdiansah H, Yaqin R I, Pristiansyah P, Umar M L and Priyambodo B H 2023 FDM-3D printing parameter optimization using taguchi approach on surface roughness of thermoplastic polyurethane parts *Int. J. Interact. Des. Manuf.* **17**

[66] Sharma K, Kumar K, Singh K R and Rawat M S 2021 Optimization of FDM 3D printing process parameters using Taguchi technique *IOP Conf. Ser.: Mater. Sci. Eng.* **1168**

[67] Gao G, Xu F and Xu J 2022 Parametric optimization of FDM process for improving mechanical strengths using Taguchi Method and response surface method: a comparative investigation *Machines* **10**

[68] Hsueh M-H, Su Y-J, Chung C-F, Hsieh C-H, Lai C-J and Chang J-F 2021 Influence of printing temperature and speed on the mechanical properties of 3D-printed PETG parts *Smart Des. Sci. Technol.* (CRC Press) 104–10

[69] Wang P, Zou B, Ding S, Li L and Huang C 2021 Effects of FDM-3D printing parameters on mechanical properties and microstructure of CF/PEEK and GF/PEEK *Chinese J. Aeronaut.* **34** 236–46